Nonlinear Regimes of Baroclinic Boundary Currents

XAVIER J. CAPET

University of California, Los Angeles, Los Angeles, California

XAVIER J. CARTON

Laboratoire de Physique des Océans, IFREMER, Brest, France

(Manuscript received 3 June 2003, in final form 8 January 2004)

ABSTRACT

A process study is conducted on the evolution of boundary currents in a two-layer quasigeostrophic model on the f plane. These currents are composed of two strips of uniform potential vorticity (PV), one in each layer, and both hugging the coast. Coastal water separation (''detrainment'') through baroclinic instability and topographic perturbation is examined. It is shown that the key characteristics of the flow finite-amplitude destabilization can be explained with the help of a linear quantity—the critical amplitude A_c—that refers to the location of the line (often called critical layer) where the phase speed of the growing perturbation is equal to the unperturbed flow velocity. Notably, prediction on PV front breaking location is made possible. Different detrainment regimes (i.e., the way fragments of the boundary current are isolated and detached from the initially rectilinear core—e.g., filament formation, eddy shedding) are also identified, related to various A_c value ranges, and compared with observed oceanic events.

1. Introduction

Boundary currents play an essential role in the mesoscale variability of the ocean. They can expel vortices and filaments seaward, thus participating in the mixing of heat, salt, and chemical (or biological) species in the open ocean. Filaments are a common feature of boundary currents. They lead to rapid mixing between adjacent waters (e.g., coastal and oceanic waters) because their coherence is weak. In contrast, coherent mesoscale vortices have a long lifetime and complex dynamics, and so they induce transport of water properties over large scales. The noticeable impact of eddies on large-scale heat and salt transport raises a particular interest in understanding their formation mechanisms.

The destabilization of ocean currents arises from intrinsic instability, external forcing (e.g., topography), or a combination of both. This has been the subject of many theoretical studies (Pratt and Stern 1986; Nof 1991; Pichevin and Nof 1997; Shimada and Kubokawa 1997). When limited to small-amplitude perturbations (linear theory) the destabilization problem is more easily tractable, and fundamental results have been obtained in this framework. The Charney–Stern criterion (Charney and Stern 1962) gives a necessary condition for linear instability to develop. Linear growth rates and most unstable wavelengths have been derived for a variety of geophysical flows whether highly idealized (Charney 1947; Phillips 1954; Ikeda 1983; Smeed 1988) or more realistic (Barth 1994). Also Pullin (1981) and Viera and Grimshaw (1994) show that wave breaking of weakly perturbed flows occurs when meanders reach a critical layer (Grimshaw and Yi 1991), whose location can be estimated through a linear calculation. Following their approach, we define the critical amplitude A_c, which is related to the location where the phase speed of a small-amplitude perturbation is equal to the fluid mean velocity. The use of this quantity by Viera and Grimshaw (1994) is limited to stable locally perturbed flows, which is consistent with the underlying linear calculation. To our knowledge, no attempt has been made to extend the range of the use of A_c to more complex cases (e.g., when the currents are stratified and potentially unstable). This is the subject of the present study.

We consider the first stage in the destabilization of rectilinear flows; this stage extends from the initially weakly perturbed state until a wave breaking occurs. Conceived as a proof of concept, this study focuses on a set of comparable boundary flows in a two-layer fluid (i.e., all currents are intensified in the upper layer and have identical maximum velocity), but that cover a wide range of A_c values, to assess the sensitivity of the flows' unstable evolution to this quantity. Only baroclinic in-

Corresponding author address: Dr. Xavier J. Capet, IGPP UCLA, 405 Charles E. Young Drive, Los Angeles, CA 90095-1567.
E-mail: capet@atmos.ucla.edu

stability is present in our study.[1] We neglect topography and the earth's curvature (no β effect). The potential vorticity (PV) is chosen as piecewise constant with only one PV front per layer. Thus, the system has two unstable wave modes (Cushman-Roisin 1994, chapters 7 and 16; Capet et al. 2002 and references therein). This provides an analytically tractable approach to pure baroclinic instability while retaining horizontal velocity shear characteristic of jet flows. Last, we restrict our investigation to quasigeostrophic (QG) dynamics (characterized by small Rossby numbers and isopycnal deviations). The QG framework has proven its ability to capture the essential dynamics of many boundary currents, such as the Norwegian coastal current (Ikeda et al. 1989) and the California current system (Ikeda and Emery 1984). More generally, similar idealized frameworks have been widely used for theoretical studies that address the unsteady evolution of boundary currents (Shimada and Kubokawa 1997; Send 1989; Grimshaw and Yi 1991; Viera and Grimshaw 1994). Indeed, they allow simple linear calculations (of which we make extensive use), while retaining important dynamical ingredients of boundary current evolutions. Our focus is on the evolution of the upper-layer current, for which comparison with data (e.g., from satellites) is easier, but the results we obtain equally apply to deep currents when neglecting the bottom slopes (by symmetry of the QG equations).

This study is organized as follows. First, the model equations are recalled, their implementation is described, and linear calculations are detailed (section 2). In the following sections we stress the relationship between unstable evolution of boundary currents and their associated critical amplitude. Two different ways are considered to trigger the instability: an initial small-amplitude sinusoidal wave corresponding to the most unstable wavelength (section 3) and a localized topographic depression playing the role of a bottom irregularity (section 4). Relevance and limitations of our results with respect to previous studies and to oceanic applications are finally discussed in section 5.

2. Configuration, model, and equations

a. Configuration

We consider a model with two homogeneous layers of depth H_1 (upper layer) and H_2 (lower layer) at rest (Fig. 1); g' denotes the reduced gravity associated with the interfaces between these layers. We assume a constant Coriolis frequency f_0 (the currents and their perturbations always keep a limited spatial extent); the internal deformation radius associated with this configuration is defined by

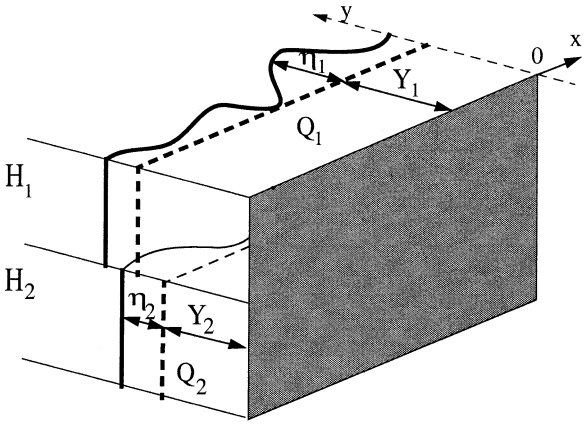

FIG. 1. Model configuration (perspective view). We consider a two-layer model with a constant PV strip against the eastern boundary in each layer. Notations are defined in the text.

$$R_d^2 = \frac{g' H_1 H_2}{f_0^2 (H_1 + H_2)}.$$

The domain is a half plane closed by a vertical wall. We consider coastal currents intensified near this wall (located at $y = 0$; Fig. 1) and associated with uniform PV anomalies in each layer. The magnitude and initial width of these PV strips are (Q_1, Y_1) and (Q_2, Y_2) for layers 1 and 2, respectively. The associated (longshore) velocities are $U_1(y)$ and $U_2(y)$.

b. Equations

As stated above, all flow investigations are limited to QG dynamics. Quasigeostrophic equations are nondimensionalized using the baroclinic radius of deformation R_d as the horizontal length scale. A time scale is also defined using the maximal upper-layer velocity $U_1^{(\max)}$, namely, $T = R_d/U_1^{(\max)}$, so that the maximum velocity of the upper current is equal to unity in the model. Consistently, the scaling for vorticity is chosen to be $1/T$. The nondimensional equations of motion are then (see Pedlosky 1987, his section 6.16)

$$\partial_t \mathrm{PV}\, A_k + J(\Psi_k, \mathrm{PV}\, A_k) = 0 \qquad k = 1, 2, \quad \text{(1a)}$$

where Ψ_k is the streamfunction in layer, PV A_k is the PV anomaly (or quasigeostrophic PV) and is given by

$$\mathrm{PV}\, A_1 = \nabla^2 \Psi_1 + F_1(\Psi_2 - \Psi_1) \qquad \text{and} \quad \text{(1b)}$$

$$\mathrm{PV}\, A_2 = \nabla^2 \Psi_2 + F_2(\Psi_1 - \Psi_2) + f_0 T h_b / H_2, \quad \text{(1c)}$$

and $J(A, B) = \partial_x A \partial_y B - \partial_x \partial_y A$ is the Jacobian of A and B; t is the nondimensional time; x and y are the nondimensional coordinates; $F_i = f_0^2 R_d^2 / g' H_i$, $(i = 1 \ldots 2)$ are the nondimensional Froude numbers [$F_i = H_{3-i}/(H_1 + H_2)$ in our scaling]; and h_b accounts for a bottom topography anomaly [by nature of the QG equations, $\max(h_b)/H_2 < 1$].

[1] In fact, it has been identified as the dominant type of instability involved in several eastern boundary currents' destabilization (Thomson and Gower 1998; Griffith and Pearce 1985b).

c. Initial state and parameters

In each layer ($k = 1, 2$), the PV anomalies $PV\,A_k$ are piecewise constant

$$\text{PV } A_k = \begin{cases} 0 & \text{if } y > Y_k \\ Q_k & \text{if } y \le Y_k. \end{cases}$$

In Capet et al. (2002), the initial streamfunction and velocity field associated with a more general configuration have been analytically derived. For the whole study, we fix the velocity maximum in the upper layer $U_1^{(\max)}$ as well as R_d, H_1/H_2 and Y_1/Y_2; two degrees of freedom are then left that we choose to be Q_1 and Q_2. We further restrict our attention to a range of flows that verify the following additional constraints:

- Lateral countercurrents in the upper layer are moderate; that is, $U_1^{(\min)}/U_1^{(\max)} > -0.4$ and the total transport in the upper layer ($\int_y U_1\,dy$) has the same sign as $U_1^{(\max)}$.
- Lower-layer currents are weaker than upper-layer currents, $|U_2^{(\max)}|/|U_1^{(\max)}| < 0.7$.

For simulations and numerical applications, we also choose the numerical values:

$$f_0 = 10^{-4}\ \text{s}^{-1}, \qquad R_d = 15\ \text{km}, \qquad H_1 = 200\ \text{m},$$

$$H_2 = 800\ \text{m}, \qquad U_1^{(\max)} = +0.35\ \text{m s}^{-1}, \text{ and}$$

$$Y_1 = Y_2 = 2.5R_d.$$

This combination of values is representative of well-defined upper-intensified prograde[2] flows. Apart from being roughly consistent with the oceanic applications we intend to make (section 5), these choices make our parameter space reasonable [the parametric study only bears on different values for (Q_1, Q_2) inside the white central area of Fig. 2]. A sensitivity investigation has shown that our general conclusions are not affected by the numerical values set in this section.

d. Numerical model

A finite-difference code is used to implement Eqs. (1a)–(1c) numerically (Holland 1978). It implies the addition of weak biharmonic viscosity to the right-hand side of Eq. (1a) to remove enstrophy accumulation near the grid scale. Since the PV of the flow is piecewise constant, a weak smoothing of the initial state is also required. The model domain is a channel either with periodic boundary conditions (section 3), or with inflow–outflow boundary conditions (section 4). A contour dynamics code (Dritschel and Ambaum 1997; Capet et al. 2002) would be more suited to handle potential vorticity fronts, but they do not offer as yet versatile boundary conditions. We carefully checked (by comparing the results of both finite-difference and contour dynamics codes, in periodic configuration) that the presence of a second longshore wall (far enough from the dynamically active area) as well as PV front smoothing and biharmonic viscosity required by our finite-differences model do not alter the physical outcome of the numerical simulations (see also Corréard and Carton 1999). Domain width and length vary, but the grid mesh size is always $R_d/9$ (eddy resolving).

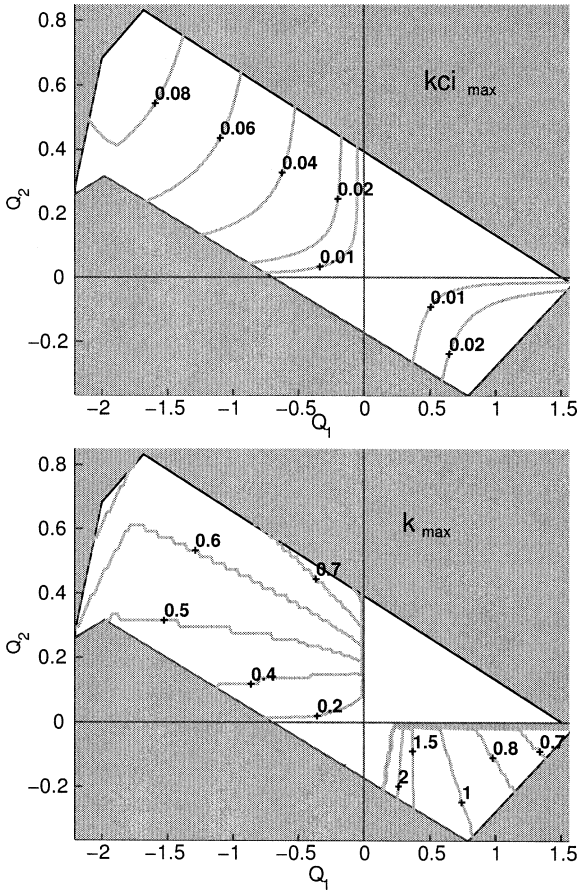

FIG. 2. Nondimensional linear instability characteristics; for a given flow, (top) $kci_{\max}$ is the maximal growth rate over all wavenumbers and (bottom) $k_{\max}$ is the corresponding wavenumber.

e. Linear instability calculations

Since the PV gradients are concentrated into the 2 PV jump (from 0 to Q_1 in layer 1, and from 0 to Q_2 in layer 2) regions, the Charney–Stern condition for instability translate to $Q_1 = Q_2 = 0$ or $Q_1Q_2 < 0$ (Charney–Stern criterion; see section 7.10 in Pedlosky 1987). The isolated case $Q_1 = Q_2 = 0$ being stable, two quadrants of the parameter space are of interest: ($Q_1 < 0$, $Q_2 > 0$) and ($Q_1 > 0$, $Q_2 < 0$). In order to explain nonlinear evolutions, linear instability is quantified in

[2] That is, leaving the coast on their right when facing downstream. Retrograde flows are opposite and do not need to be treated explicitly because of the full symmetry of the problem with regard to the longshore direction in QG.

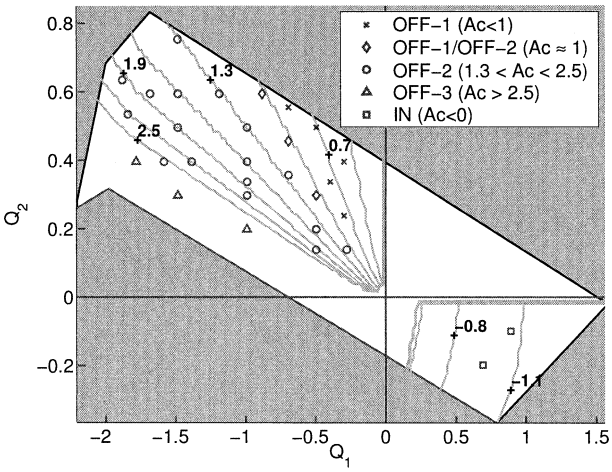

FIG. 3. Upper-layer nonlinear regimes superimposed on A_c isolines (interval 0.3) for a small initial wave perturbation. The symbols indicate whether OFF-1 (×), OFF-2 (○), intermediate regime between OFF-1 and OFF-2 (◇), OFF-3 (△), or IN regime (□) is observed.

these regions. The general linear stability analysis for piecewise PV flows is given in Capet et al. (2002). It leads to a linear system $A\eta = c\eta$, where $\eta = (\eta_1, \eta_2)$ is the PV front interface deviation vector (Fig. 1); c the phase speed of this perturbation (scalar); and A (2 by 2 matrix) is given in the appendix. The corresponding dispersion relation is quadratic. Solving it yields the most unstable wavenumber $k_{\max}$, and the associated growth rate $kci_{\max}$ for flows corresponding to our PV distribution. Overall, the growth rate $kci_{\max}$ (Fig. 2) increases with $|Q_1 - Q_2|$, and the most unstable wavenumber (Fig. 2) corresponds to wavelengths on the order of 3–$12R_d$, consistent with the baroclinic nature of the instability. Asymmetry between the quadrants ($Q_1 < 0$, $Q_2 > 0$) and ($Q_1 > 0$, $Q_2 < 0$) can be explained by differences in terms of unstable wave coupling (Capet et al. 2002).

Following Viera and Grimshaw (1994), we also evaluate, where it exists, the critical amplitude A_c (in the upper layer where our focus is); A_c is defined as the value of η_1 such that the phase speed of the most unstable wavelength is equal to the velocity of the basic flow $U_1(Y_1 + \eta_1)$. It refers to the location of a critical layer in the flow. Note that $A_c > 0$ corresponds to a critical layer located off the PV front; A_c is shown in Fig. 3 (solid lines). In the ($Q_1 < 0$, $Q_2 > 0$) quadrant, critical layers are located off the PV fronts, and A_c ranges from $0.7R_d$ to $2.5R_d$ in most of this quadrant, with

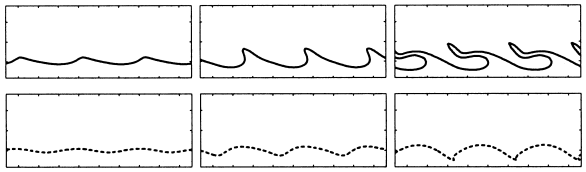

FIG. 4. Nonlinear evolution of the (top) upper (solid line) and (bottom) lower (dashed line) PV fronts corresponding to ($Q_1 = -0.70$, $Q_2 = 0.55$), over a flat bottom. Times $t = 40$, 65, and 90 are shown from left to right. The distance between two consecutive ticks is $3R_d$. This evolution illustrates the OFF-1 regime. With the numerical values specified in section 2c, filamentation occurs after 35 days.

undefined values in its lower part (no critical layer). In contrast, critical layers are situated inshore of the PV front in the ($Q_1 > 0$, $Q_2 < 0$) quadrant with $|A_c|$ on the order of the deformation radius away from the axes $Q_1 = 0$ and $Q_2 = 0$.

3. Current destabilization over a flat bottom

In this section, the flows are initially weakly perturbed on their most unstable wavelength (the domain length is adjusted to be equal to two or three wavelengths). Baroclinic instability is the only process that can amplify this initial perturbation, generate finite-amplitude mesoscale structures, and possibly yield to vortex or filament formation.

Thirty numerical simulations have been performed for various (Q_1, Q_2) values, and the results of the nonlinear evolutions in the upper layer are summarized in Fig. 3. Areas close to the axes in the parameter space have not been specifically investigated to avoid lengthy simulations from very weak growth rates; furthermore, in long simulations, viscous effects come into play. With this precaution, we checked that the use of a contour dynamics code does not change our results. These results are described and then interpreted using critical-amplitude calculations.

a. Description of unstable evolution regimes

Four flow evolution regimes are identified with specific locations in the parameter space. Their label, location in (Q_1, Q_2) space, and brief description are given in Table 1. In the upper-right corner of the ($Q_1 < 0$, $Q_2 > 0$) quadrant, meander amplification through baroclinic instability leads to offshore filamentation (OFF-1 regime) as shown in Fig. 4 for ($Q_1 = -0.70$, $Q_2 = 0.55$). The perturbation cannot expand very far away

TABLE 1. Nonlinear regimes obtained through destabilization of the boundary currents.

Regime	Description	Location
OFF-1	Filamentation off the PV front	Upper right of ($Q_1 < 0$, $Q_2 > 0$)
OFF-2	Eddy formation off the PV front	Center of ($Q_1 < 0$, $Q_2 > 0$)
OFF-3	Large meanders without detachment	Lower part of ($Q_1 < 0$, $Q_2 > 0$)
IN	Filamentation within the PV front	($Q_1 > 0$, $Q_2 < 0$)

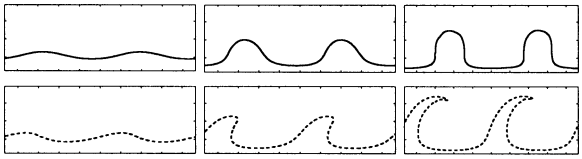

FIG. 5. Similar to Fig. 4 for ($Q_1 = -1.0$, $Q_2 = 0.16$) except that a mode-2 perturbation is initially introduced. Times $t = 85$, 130, and 175 are represented. This evolution illustrates the OFF-3 regime (A_c is undefined for this flow). After 70 days no clear detachment has occurred from the boundary current. (Note that the actual computation domain is much larger in the cross-shore direction than shown here.)

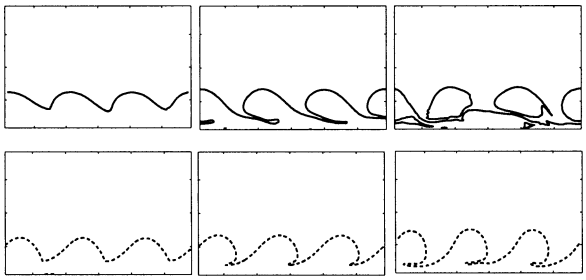

FIG. 7. Similar to Fig. 4 for ($Q_1 = 0.60$, $Q_2 = -0.20$). Times $t =$ 215, 260, and 300 are shown. This evolution illustrates the IN regime.

from the initial PV front position since the offshore part of the meanders steepens rapidly in the upstream direction, and filaments containing inshore water are formed. In contrast, in the lowest part of the same quadrant, large meanders are formed (in the upper layer) as the result of complete linear growth of the perturbation, not marked by wave steepening or breaking. In the lower layer, weaker PV is wrapped around the strong upper PV poles. The evolution shown in Fig. 5 for ($Q_1 = -1.0$, $Q_2 = 0.16$) is representative of this regime (OFF-3 regime). Between these two areas, another dynamical regime exhibits wave steepening as in the case OFF-1, but only after the perturbation is well developed. A significant amount of upper PV is therefore trapped when the wave steepening process results in PV cutoff. Thus, mesoscale eddies (i.e., with a radius much greater than R_d) are formed [OFF-2 regime; see Fig. 6 for ($Q_1 = -1.90$, $Q_2 = 0.63$)].

Note that no real discontinuity exists between these three regimes that we somewhat arbitrarily distinguished for clarity of the discussion. For example, intermediate evolutions between OFF-1 and OFF-2 are found ($\diamond$ in Fig. 3) where swollen filaments of thickness close to R_d are generated.

We finally mention the fourth regime (IN regime), which coincides with the ($Q_1 > 0$, $Q_2 < 0$) region of the parameter space. The evolution of ($Q_1 = +0.60$, $Q_2 = -0.20$) shown on Fig. 7 illustrates this regime. The process of PV isolation here is different from those previously described. As the perturbation grows, wave steepening occurs, but it takes place inside the coastal current strip and yields to a filament of zero PV offshore water. Seaward excursions of coastal water are very limited: the boundary current PV is splitted into a vortex row, but these vortices remain at the coast.

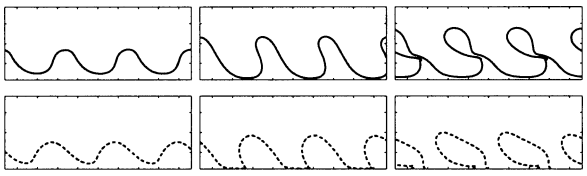

FIG. 6. Similar to Fig. 4 for ($Q_1 = -1.90$, $Q_2 = 0.63$). Times $t =$ 45, 55, and 65 are shown. This evolution illustrates the OFF-2 regime (eddy detachment that occurs after a 25-day growing period).

b. Unstable evolutions and critical amplitude

Locations where the flow produces filamentation or cutoff correspond to velocity saddle points [i.e., points where, in the wave reference frame, the fluid velocity vanishes and the velocity field is locally hyperbolic; e.g., see the streamfunction and velocity field during meander cut off for ($Q_1 = -1.50$, $Q_2 = 0.75$) on Fig. 8]. Initially, the fluid with zero velocity (in the wave frame) is located on the critical layers at a distance A_c from the PV front. Although meander amplification changes the position of these stagnation points, we expect A_c to give a reasonable first approximation of the location where cutoff takes place, at least when $|A_c|$ is small in comparison with R_d. Indeed, for small $|A_c|$, front steepening and further nonlinear processes occur early during wave growth, that is, when linear approximation remains accurate enough. The plot of A_c versus the observed location of the saddle point (Fig. 9) for the OFF-1 and OFF-2 regime flows justifies this statement. A satisfac-

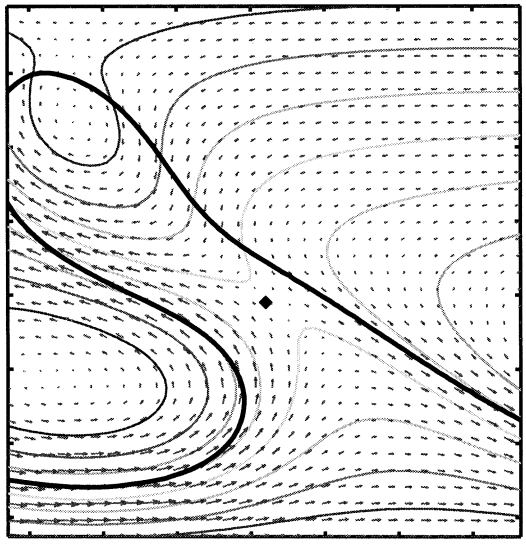

FIG. 8. Instantaneous upper PV front (thick line), streamlines (thin lines), and corresponding velocities for ($Q_1 = -1.50$, $Q_2 = 0.75$). Streamlines and velocities are calculated in the unstable wave reference frame. A saddle (hyperbolic) point is present (small square), and cutoff occurs around its location. The figure is zoomed in on the isolation region. The distance between two consecutive ticks is R_d.

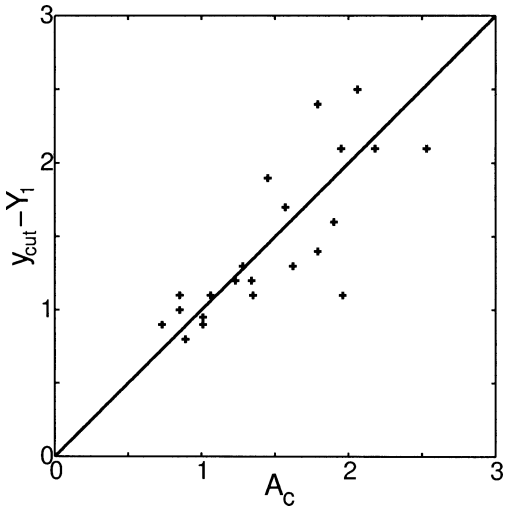

FIG. 9. Critical amplitude A_c vs $y_{cut} - Y_1$ where (x_{cut}, y_{cut}) is the position of the saddle point during the cutoff process. The line of perfect agreement between linear theory and nonlinear result (i.e., $A_c = y_{cut} - Y_{11}$) is also plotted.

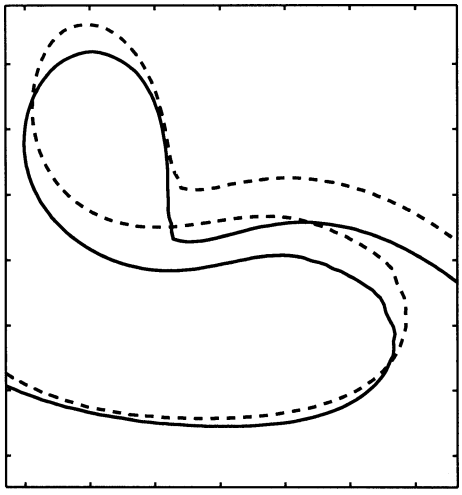

FIG. 10. Upper PV front for $(Q_1 = -1.50, Q_2 = 0.75)$ at $t = 60$ (solid line) and for $(Q_1 = -0.70, Q_2 = 0.35)$ at $t = 120$ (dashed line) superimposed after an appropriate translation along the x axis. This figure is zoomed in as in Fig. 8. Both flows have an A_c value of $1.3R_d$ and very similar detached structures.

tory agreement between observed and predicted values is obtained up to $A_c = 1.5$.[3]

Beyond $A_c = 1.5$, there is an important scattering but the qualitative use of A_c remains of interest. Flows corresponding to the OFF-3 regime have evolutions consistent with their values of A_c: the absence of saddle points and cutoff during flow destabilization relates to large values of A_c ($\gtrsim 2.5R_d$) or undefined values of A_c (no critical layer present initially). Similarly there is a consistency between negative A_c values of ($Q_1 > 0$, $Q_2 < 0$) flows and their nonlinear evolution (IN regime). Therefore the different physical regimes identified (see Table 1) can all be characterized by different values of A_c. Values bounding these regimes are likely to be specific to our study and thus somewhat arbitrary, but the underlying kinematic mechanism is fully general.

In view of the similarity between the detached eddies associated with identical A_c (Fig. 10), it is finally tempting to relate quantitatively the size of the detached structures (if any) to A_c. We focus on regime OFF-2 since size differences between eddies of the IN regime are small and their separation from the boundary current is not always very clear. To eliminate the dependency of eddy size on the unstable wavelength, we define the ejection rate Ej as the ratio between the quantity of PV contained in the ejected eddy and the amount of PV initially present in one wavelength of the boundary current $[(2\pi Q_1/k_{max})Y_1]$. Figure 11 represents the values obtained for Ej/A_c superimposed on A_c isolines. Following A_c isolines from the origin to the left-hand side of the quadrant, an increase in Ej/A_c is noticeable. It might be explained by the corresponding large increase of the growth rate (see Fig. 2). However, the standard deviation of Ej/A_c around its mean (0.20) is very small (2.7×10^{-2}) in regard to the variations of E_j itself (eddy radii range over $1.2–2.5R_d$). It means that the eddy size increases roughly linearly with A_c, and this gives further evidence that the detrainment is strongly controlled by A_c.

4. Current destabilization over a bathymetric anomaly

a. Idealized bathymetry

In the ocean current meanders are often triggered and shaped by flow–bathymetry interactions. In such a sit-

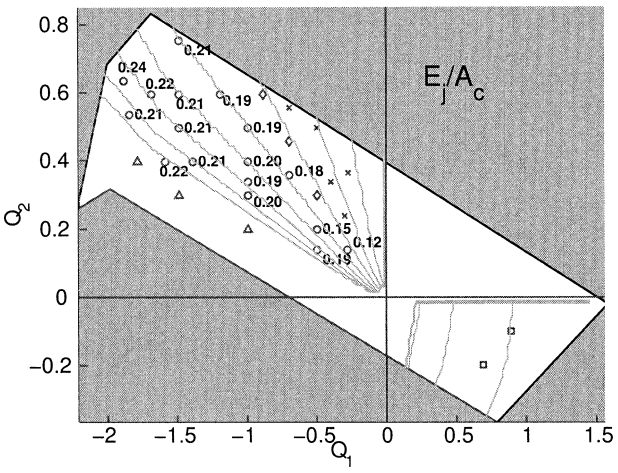

FIG. 11. Values of E_j/A_c (for OFF-2 regime runs) superimposed on lines of equal critical amplitude (interval 0.3). Symbols correspond to those of Fig. 3.

[3] When A_c is <0 (IN regime), the agreement is also good (not shown) but no flow of the parameter space has A_c values lower than $-1.3R_d$.

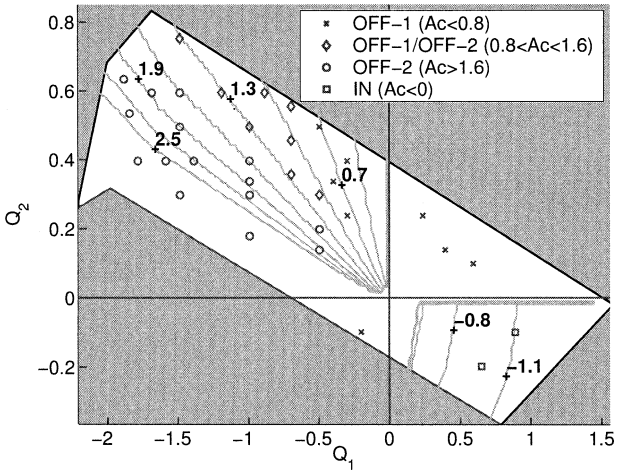

FIG. 12. Nonlinear regimes (resulting from a permanent perturbation due to an $\mathcal{R} = 1$ depression) superimposed on lines of equal critical amplitude (lines and symbols as in Fig. 3).

uation, the strong symmetry and regularity properties inherent to a sinusoidal perturbation growth (section 3) are no longer present. In this section we consider the case in which a depression contributes to boundary current destabilization in order to assess the validity of our previous results about A_c with more complex perturbations.

The bathymetric anomaly is a depression defined by $h_c(x, y) = h_{c0} \exp\{-[x^2 + (y - Y_1)^2]/R_d^2\}$. Changing the shape of topography anomaly (e.g., trench, bump) does not affect the results presented below; h_{c0} is chosen such that Q_2 and the PV associated with the depression [topographic PV in Eq. (1c)] are of equal strength [i.e., the ratio $\mathcal{R} = f_0 T h_{c0}/(H_2 Q_2) = 1$]. For the flows we consider, this value of $\mathcal{R}$ satisfies the QG hypotheses. The topographic PV is included in the lower-layer PV, which remains unchanged at $t = 0$ (equal to Q_2 over the strip). The initial flow velocities are calculated from this PV distribution and are thus different from those of the previous section. The domain length has been set long enough (up to $50R_d$) to allow unsteady phenomena to fully develop before reaching inflow-outflow boundaries.

b. Unstable evolutions and critical amplitude

Subject to finite-amplitude perturbations, even linearly stable flows belonging to the ($Q_1 < 0$, $Q_2 < 0$) and ($Q_1 > 0$, $Q_2 > 0$) can be deformed. For a comparable configuration, Viera and Grimshaw (1994) demonstrated the relevance of linear calculations to predict where PV front breaking takes place. This is, therefore, not developed here.

For weak to moderate topographic anomalies ($\mathcal{R} = 1$), the detrainment regimes for linearly unstable flows are summarized in Fig. 12. In each case, a perturbation is rapidly produced in the lower layer due to the adjustment of the flow to the presence of the depression. Layer coupling through the density interface allows the perturbation to be transmitted upward; baroclinic instability amplifies this perturbation that is a superposition of wavelengths over a wide range, from domain size down to the grid scale. Therefore, the details of flow evolutions differ from those observed in section 3. In particular, the strong initial interaction between the depression and the flow creates a single dominant meander. [See the evolution of cases ($Q_1 = -1.90$, $Q_2 = 0.63$) or ($Q_1 = 0.60$, $Q_2 = -0.20$) in Figs. 13 and 14.] Furthermore, small-scale structures always exist in the perturbation [contrast the lower PV structures for ($Q_1 = -1.90$, $Q_2 = 0.63$) in Figs. 13 and 6]. This confirms that the currents evolution is strongly affected by the depression–flow interaction that is not taken into account in our linear calculation of A_c. As a consequence, the agreement between the actual cutoff location and the linearly predicted one (A_c) is weaker when compared with section 3. For example, the flow ($Q_1 = -1.90$, $Q_2 = 0.63$) finally detaches an eddy, but the cutoff process occurs far away from the coast ($\approx 9R_d$) when compared with the A_c prediction ($4.45R_d$) and also when compared with what occurred during the simulation with no bottom topography ($\approx 4.5R_d$; see Fig. 6 and Fig. 13). Furthermore, the relation between the size of detached eddies and A_c is not clear anymore (not shown).

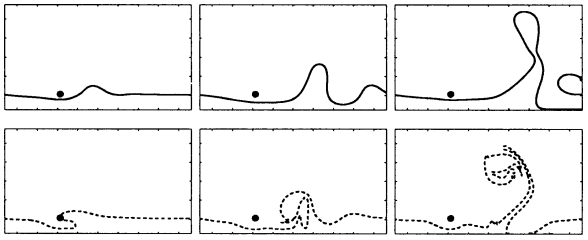

FIG. 13. Nonlinear evolution of the (top) upper (solid line) and (bottom) lower (dashed line) PV fronts corresponding to ($Q_1 = -1.90$, $Q_2 = 0.63$). Times $t = 15$, 40, and 75 are shown. A 128-m-deep depression ($\mathcal{R} = 1$) is centered on the small black dot. The distance between two consecutive ticks is $3R_d$.

However, it is noteworthy that flow regimes are essentially unchanged in comparison with those of section 3 (see Figs. 12 and 3). Low positive (respectively, high positive) A_c values are still associated with filamentation (OFF-1) (respectively, eddy separation, OFF-2) regimes. Negative A_c values still correspond to inner filamentation that occurs in the quadrant ($Q_1 > 0$, $Q_2 < 0$)

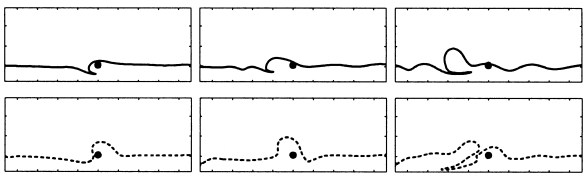

FIG. 14. Similar to Fig. 13 for ($Q_1 = 0.60$, $Q_2 = -0.20$). Times $t = 45$, 85, and 175 are shown. The depression is 40 m deep ($\mathcal{R} = 1$).

(Fig. 14). We attribute this qualitative agreement to the moderate effect of the depression on velocities: the flow–depression interaction mainly triggers the instability when the baroclinic coupling is permanent. Increasing $\mathcal{R}$ (or the depression size) reinforces the effect of the depression so that A_c based classification has little significance for $\mathcal{R} \gtrsim 2.5$ (not shown). Such large $\mathcal{R}$ cases should, however, be considered in the shallow-water framework since they tend to break the QG assumptions.

5. Discussion

a. Summary

There has been longstanding experience that linear calculations of the most unstable wavelength and growth rate associated with an unstable flow provide useful information even after the initial linear growth stage is over (Ikeda and Apel 1981) [although growth rates are affected by nonlinearities so that other wavelengths can emerge and even dominate in some cases (Ikeda et al. 1984)]. Our numerical experiments in an idealized framework suggest that linear predictions based on the critical amplitude also hold beyond the strict linear growth stage of unstable perturbations and give reliable information on where and how nonlinear breaking of a growing perturbation occurs. This proves to be helpful in describing and even quantifying the detrainment arising from flow destabilization.

Most notably, several theoretical implications follow the results of sections 3 and 4.

1) Important work has been dedicated to explaining the generation of submesoscale vortices through specific mechanisms (D'Asaro 1988; McWilliams 1988). We emphasize here the idea that the formation of small eddies is also compatible with classical baroclinic instability. It is obtained by our numerical experiments for small positive values of A_c.
2) It is generally accepted that the destabilization of wide currents yields big eddies (e.g., Feliks and Ghil 1993). This is likely true, but the present study suggests that A_c significantly accounts for the eddy size and is not related to the current width in a straightforward way.
3) Stern and Chassignet (2000) argue that blocking waves, in particular waves induced by a topographic anomaly, can reinforce detrainment processes (e.g., lead to eddy formation instead of filamentation for a given flow). On the other hand, we found that detrainment regimes are primarily related to A_c and are essentially unchanged when the initial sinusoidal perturbation of small amplitude (section 3) is replaced by a topographic anomaly (section 4). A shallow-water model (in which more complex interactions between the flow and the topography are allowed) might be necessary for blocking waves to act effectively and to enhance the detrainment.

b. Toward experimental validation

Several differences between the real ocean and the present framework make the experimental validation and application of our results a difficult task. First, the analysis and classification of wave breaking and detrainment regimes cannot easily be approached using observations because of background turbulence, variable environments including slope and shelf, flow pulses (Stern and Chassignet 2000), coastal waves, and mixing action with surrounding waters; different types of regimes may then exist depending on ''local'' conditions. In addition, moderate barotropic instability complicates our classification of unstable evolution regimes according to A_c values (this point is currently under investigation). Furthermore, determining A_c in the ocean will require high-resolution velocity data and precise evaluation of the unstable waves' phase speed. Last, our simulations were halted when PV breaking occurred, and the ability of the different regimes to lead to water detrainment were assessed at that time. It then seems that the OFF-2 regime is the most favorable for effective eddy formation. However, further evolution could likely change this view. On the one hand, detached eddies can either move seaward (e.g., as baroclinic dipoles) or merge back into the coastal flow. On the other hand, onshore eddy rows obtained for ($Q_1 > 0$, $Q_2 < 0$) (IN regime) or large undetached meanders (OFF-3) may finally separate from the coast, particularly if the β effect is present and induces seaward eddy advection.

To conclude, we briefly discuss three boundary current destabilization events. They suggest that the unstable evolutions and detrainment regimes we obtained are also observed in nature (although our idealized framework may not be suited to modeling the evolution of these particular currents). During winter 1995, the northeast Pacific coastal current flowing northward along British Columbia and Alaska coasts destabilized and formed a row of six vortices spanning more than 1500 km [see plate 1 in Thomson and Gower (1998) and also our derived zoomed sketch in Fig. 15a]. Inshore filamentation developed during wave growth: offshore waters deeply penetrated into the coastal flow and isolated a series of vortices. This evolution *kinematically* compares to that of the IN regime (critical layer inside the current core). Note that numerical simulations (using a primitive equation model) intended to study this eddy formation event (Melsom et al. 1999) led to flow evolution that also seems to fall into IN regime classification. The destabilization of the Leeuwin Current also yields eddies that were observed on infrared images (Griffith and Pearce 1985a,b; Legeckis and Cresswell 1981). Here we focus our attention on the development of two particular features: the eddy labeled A, and the

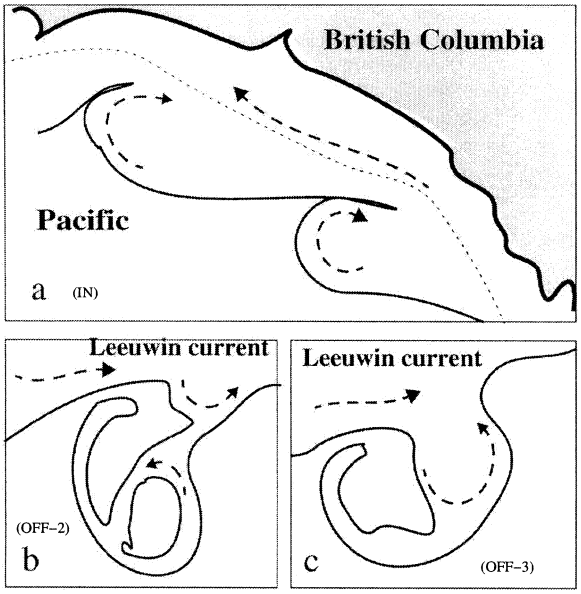

FIG. 15. Sketch of different eddy formation from boundary currents as suggested by satellite SST maps. In each case, the solid thick line indicates the approximate location of the largest temperature gradient. Arrows indicate water motion expected by the authors. (a) Part of a six-vortex string whose formation is reported by Thomson and Gower (1998). The coast (bold line), 1000-m isobath (dashed line), and land (shaded region) are represented. (b) Formation of the structure labeled ''A'' from the Leeuwin Current in Griffith and Pearce (1985a). (c) Formation of the structure labeled ''B'' from the Leeuwin Current in Griffith and Pearce (1985a).

large undetached (on the available images) structure labeled B in Griffith and Pearce (1985b). A sketch of their formation is given in Fig. 15. For structure A, temperature and velocities show a shearing process acting on the offshore part of an unstable meander as in our OFF-2 regime (critical layer outside the current core). As to structure B development, no cutoff mechanism is observed despite a meander offshore extension of 140 km from the Leeuwin Current position. In our study, flows with large A_c (OFF-3 regime, no critical layer in the flow) behave in a similar way when destabilized. Since no A_c value associated with these different destabilization episodes is computable, the relevance of A_c in the oceanic context has not been demonstrated. However, we believe that A_c provides a valuable estimate of the velocity shear encountered by finite-amplitude waves and therefore gives a kinematic insight into the breaking of baroclinically unstable flows. Validation tests involving primitive equation model simulations are now considered to further support this belief.

Acknowledgments. The first author acknowledges support from SHOM and DGA via a Ph.D. grant. Discussions with David Dritschel, Yves Morel, and Laurent Chérubin were timely and valuable. Diana McWilliams assisted in the proofreading of this manuscript.

APPENDIX

The Linear Instability Matrix

$$A = \begin{bmatrix} U_1(Y_1) & 0 \\ 0 & U_2(Y_2) \end{bmatrix} - \begin{bmatrix} Q_1(h_1 a_1^1 + h_2 b_1^1) & Q_2 h_2 (a_1^2 - b_1^2) \\ Q_1 h_1 (a_2^1 - b_2^1) & Q_2(h_2 a_2^2 + h_1 b_2^2) \end{bmatrix},$$

where

$$a_l^n = \frac{1}{2k}(e^{-k|Y_l + Y_n|} - e^{-k|Y_l - Y_n|}) \quad \text{and}$$

$$b_l^n = \frac{1}{2k_\gamma}(e^{-k_\gamma|Y_l + Y_n|} - e^{-k_\gamma|Y_l - Y_n|})$$

with $k_\gamma^2 = k^2 + 1$.

REFERENCES

Barth, J. A., 1994: Short wavelength instabilities on coastal jets and fronts. *J. Geophys. Res.,* **99,** 16 095–16 115.

Capet, X., L. Chérubin, and Y. Morel, 2002: Influence of the transport on the instability of a boundary current. *J. Phys. Oceanogr.,* **32,** 2806–2815.

Charney, J. G., 1947: The dynamics of long waves in a baroclinic westerly current. *J. Meteor.,* **4,** 135–163.

——, and M. E. Stern, 1962: On the instability of internal baroclinic jets in a rotating atmosphere. *J. Atmos. Sci.,* **19,** 159–172.

Corréard, S. M., and X. J. Carton, 1999: Formation and stability of tripolar vortices in stratified geostrophic flows. *Nuovo Cimento,* **22C,** 767–777.

Cushman-Roisin, B., 1994: *Introduction to Geophysical Fluid Dynamics.* Prentice Hall, 320 pp.

D'Asaro, E., 1988: Generation of submesoscale vortices: A new mechanism. *J. Geophys. Res.,* **93,** 6685–6693.

Dritschel, D. G., and M. H. P. Ambaum, 1997: A contour-advective semi-Lagrangian numerical algorithm for simulating fine-scale conservative dynamical fields. *Quart. J. Roy. Meteor. Soc.,* **123,** 1097–1130.

Feliks, Y., and M. Ghil, 1993: Downwelling-front instability and eddy formation in the eastern Mediterranean. *J. Phys. Oceanogr.,* **23,** 61–78.

Griffith, R. W., and A. F. Pearce, 1985a: Satellite images of an unstable warm eddy derived from the Leeuwin Current. *Deep-Sea Res.,* **32,** 1371–1380.

——, and ——, 1985b: Instability and eddy pairs on the Leeuwin Current. *Deep-Sea Res.,* **32,** 1511–1534.

Grimshaw, R., and Z. Yi, 1991: Evolution of a potential vorticity front over a topographic slope. *J. Phys. Oceanogr.,* **21,** 1240–1255.

Holland, W. R., 1978: The role of mesoscale eddies in the general circulation of the ocean—Numerical experiments using a wind-driven quasi-geostrophic model. *J. Phys. Oceanogr.,* **8,** 363–392.

Ikeda, M., 1983: Linear instability of a current flowing along a bottom slope using a three-layer model. *J. Phys. Oceanogr.,* **13,** 208–223.

——, and J. Apel, 1981: Mesoscale eddies detached from spatially growing meanders in an eastward-flowing oceanic jet using a two-layer quasi-geostrophic model. *J. Phys. Oceanogr.,* **11,** 1638–1661.

——, and W. Emery, 1984: Satellite observations and modeling of

meanders in the California Current System off Oregon and northern California. *J. Phys. Oceanogr.,* **14,** 1434–1449.
——, L. Mysak, and W. Emery, 1984: Observations and modeling of satellite-sensed meanders and eddies off Vancouver Island. *J. Phys. Oceanogr.,* **14,** 3–21.
——, J. A. Johannessen, K. Lygre, and S. Sandven, 1989: A process study of mesoscale meanders and eddies in the Norwegian coastal current. *J. Phys. Oceanogr.,* **19,** 20–35.
Legeckis, R., and G. Cresswell, 1981: Satellite observations of sea-surface temperature fronts off the coast of western and southern Australia. *Deep-Sea Res.,* **28,** 297–306.
McWilliams, J. C., 1988: Vortex generation through balanced adjustment. *J. Phys. Oceanogr.,* **18,** 1178–1192.
Melsom, A., S. D. Meyers, H. E. Hurlburt, E. J. Metzger, and J. J. O'Brien, 1999: ENSO effects on Gulf of Alaska eddies. *Earth Interactions,* **3.** [Available online at http://EarthInteractions.org.]
Nof, D., 1991: Lenses generated by intermittent currents. *Deep-Sea Res.,* **38,** 325–345.
Pedlosky, J., 1987: *Geophysical Fluid Dynamics.* 2d ed. Springer-Verlag, 710 pp.
Phillips, N. A., 1954: Energy transformations and meridional circulations associated with simple baroclinic waves. *Tellus,* **6,** 273–286.
Pichevin, T., and D. Nof, 1997: The momentum imbalance paradox. *Tellus,* **49,** 298–319.
Pratt, L. J., and M. E. Stern, 1986: Dynamics of potential vorticity fronts and eddy detachment. *J. Phys. Oceanogr.,* **16,** 1101–1120.
Pullin, D., 1981: The nonlinear behaviour of a constant vorticity layer at a wall. *J. Fluid Mech.,* **108,** 401–421.
Send, U., 1989: Vorticity and instability during flow reversal on the continental shelf. *J. Phys. Oceanogr.,* **19,** 1620–1633.
Shimada, K., and A. Kubokawa, 1997: Nonlinear evolution of linearly unstable barotropic boundary currents. *J. Phys. Oceanogr.,* **27,** 1326–1348.
Smeed, D. A., 1988: Baroclinic instability of three-layer flows, part 1. *J. Fluid Mech.,* **194,** 217–231.
Stern, M., and E. Chassignet, 2000: Mechanism of eddy separation from coastal currents. *J. Mar. Res.,* **58,** 269–295.
Thomson, R. E., and J. F. Gower, 1998: A basin-scale oceanic instability event in the Gulf of Alaska. *J. Geophys. Res.,* **103,** 3033–3040.
Viera, F., and R. Grimshaw, 1994: Topographic forcing of mesoscale phenomena: Filamentation, vortex formation, and eddy detachment. *J. Phys. Oceanogr.,* **24,** 1433–1448.